

See discussions, stats, and author profiles for this publication at: <https://www.researchgate.net/publication/263962540>

Highly Active, Nonprecious Metal Perovskite Electrocatalysts for Bifunctional Metal–Air Battery Electrodes

ARTICLE *in* JOURNAL OF PHYSICAL CHEMISTRY LETTERS · APRIL 2013

Impact Factor: 7.46 · DOI: 10.1021/jz400595z

CITATIONS

55

READS

173

6 AUTHORS, INCLUDING:



[William G. Hardin](#)

University of Texas at Austin

9 PUBLICATIONS 223 CITATIONS

SEE PROFILE



[Xiqing Wang](#)

Nanotek Instruments, Inc.

55 PUBLICATIONS 2,250 CITATIONS

SEE PROFILE

Highly Active, Nonprecious Metal Perovskite Electrocatalysts for Bifunctional Metal–Air Battery Electrodes

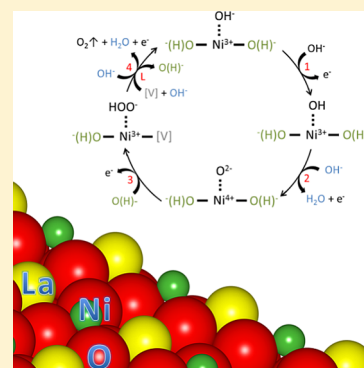
William G. Hardin,^{1,∇} Daniel A. Slanac,^{†,∇} Xiqing Wang,[#] Sheng Dai,[#] Keith P. Johnston,^{*,†,§,⊥} and Keith J. Stevenson^{*,‡,§,⊥}

[†]Department of Chemical Engineering (1 University Station C0400), [‡]Department of Chemistry and Biochemistry (1 University Station A5300), [§]Center for Electrochemistry, and [⊥]Texas Materials Institute, The University of Texas at Austin, Austin, Texas 78712, United States

[#]Chemical Sciences Division, Oak Ridge National Laboratory, Oak Ridge, Tennessee 37831, United States

S Supporting Information

ABSTRACT: Perovskites are of great interest as replacements for precious metals and oxides used in bifunctional air electrodes involving the oxygen evolution reaction (OER) and oxygen reduction reaction (ORR). Herein, we report the synthesis and activity of a phase-pure nanocrystal perovskite catalyst that is highly active for the OER and ORR. The OER mass activity of LaNiO_3 , synthesized by the calcination of a rapidly dried nanoparticle dispersion and supported on nitrogen-doped carbon, is demonstrated to be nearly 3-fold that of 6 nm IrO_2 and exhibits no hysteresis during oxygen evolution. Moreover, strong OER/ORR bifunctionality is shown by the low total overpotential (1.02 V) between the reactions, on par or better than that of noble metal catalysts such as Pt (1.16 V) and Ir (0.92 V). These results are examined in the context of surface hydroxylation, and a new OER cycle is proposed that unifies theory and the unique surface properties of LaNiO_3 .



SECTION: Energy Conversion and Storage; Energy and Charge Transport

Rechargeable metal–air batteries that utilize aqueous alkaline electrolytes may be designed with nonprecious metals to offer high theoretical specific energy densities, for example, 1084 W h/kg for Zn–air. For such systems, including alkaline electrolyzers and fuel cells, catalyst bifunctionality is a key requirement for rechargeable and/or reversible systems. However, applications have been limited by the sluggish kinetics of the oxygen evolution (OER) and oxygen reduction (ORR) reactions.^{1–4} In alkaline conditions, current state of the art OER and ORR catalysts utilize expensive precious metals such as IrO_2 and Pt, respectively.^{5,6} Interestingly, precious-metal-free perovskite oxides (ABO_3 , where A is a rare earth and B a transition metal) display bifunctional activity for both the OER and ORR. In each reaction, the activities display a volcano-type relationship with respect to the number of electrons in the e_g orbital of the B site atom.^{7,8} In particular, LaNiO_3 lies near the top of both ORR and OER volcano plots and, furthermore, has been shown to display metal-like conductivities. Consequently, OER specific activity, up to 370 $\mu\text{A}/\text{cm}^2$,^{9,10} of low surface area LaNiO_3 approaches the benchmark value for high surface area IrO_2 of 500 $\mu\text{A}/\text{cm}^2$.^{5,8} However, recently reported mass activities for LaNiO_3 are more than 10× lower than those of precious metal oxides, presumably due to the inability of current synthetic schemes to achieve both high perovskite phase purity and high surface area (<4 m^2/g for LaNiO_3 versus >70 m^2/g for IrO_2).^{5,7,8}

Perovskite catalysts are typically formed by ball milling of bulk materials to obtain particles that are >200 nm to several micrometers in diameter.^{11,12} An alternative strategy is to synthesize amorphous perovskite nanoparticles with bottom-up approaches by sol–gel methods,^{12–14} reactions in reverse micelles,^{15–17} coprecipitation hydrolysis processes,^{18–20} and hydrothermal routes.^{21,22} Nanoparticles as small as ~10 nm may be synthesized by precipitation of metal hydroxides in the presence of capping ligands.^{14,20} However, due to disparities in hydrolysis rates for systems with two or more metals^{12,22} and undesired side reactions with carbon supports at high temperatures ($\geq 600^\circ\text{C}$),^{13,14,16} phase impurities have been observed and have led to low mass activities. Furthermore, calcination steps required to form crystalline perovskites result in significant coalescence and typically produce low surface area particles ranging from 200 nm to 1 μm or greater.^{13,14,21} Phase purity and high surface area are also important requirements for other applications of perovskites such as solid oxide fuel cell electrodes and membranes, chlor-alkali and water electrolysis electrodes, capacitors, sensors, and nonvolatile memory.^{22–24} Thus, key challenges remain to synthesize phase-pure materials while minimizing agglomeration during calcination for the formation of catalysts with high electrocatalytic mass activities.

Received: March 18, 2013

Accepted: March 27, 2013

Published: March 27, 2013



Herein, we present a general scheme for synthesis of phase-pure, catalytically active LaNiO_3 that displays exceptionally high OER mass activities and a strong OER/ORR bifunctional character when supported on nitrogen-doped carbon (NC). A key advance was to prepare uniform 25 nm nanoparticle dispersions in aqueous solution via rapid simultaneous hydrolysis of both La^{3+} and Ni^{2+} nitrates by reverse phase arrested growth precipitation, which, when calcined, form nearly phase-pure LaNiO_3 nanocrystalline catalysts. Scanning electron microscopy (SEM), X-ray diffraction (XRD), dynamic light scattering (DLS), and X-ray photoelectron spectroscopy (XPS) indicated that calcination of 25 nm amorphous mixed metal hydroxide particles yielded 20–50 nm phase-pure aggregates of relatively distinct primary nanoparticles that exhibit significant surface hydroxylation and possess a surface area of $\sim 11 \text{ m}^2/\text{g}$. Coalescence was mitigated by the large interparticle spacing in highly open, low fractal dimension nanoparticulate powders produced by rapid freeze-drying enabled by thin film freezing followed by lyophilization. LaNiO_3 prepared by this method, which will be referred to as “freeze-drying”, has been designated as “nanostructured” LaNiO_3 (ns LaNiO_3) due to the morphology observed in Figure 1A.

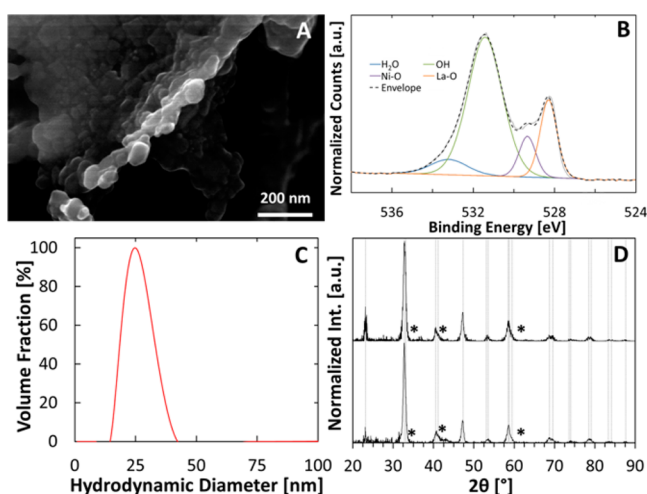


Figure 1. (A) SEM image of calcined LaNiO_3 after freeze-drying. (B) Deconvoluted O 1s core-level spectrum of freeze-dried LaNiO_3 . (C) DLS size distribution curve for as-synthesized amorphous hydroxide precursor particles, indicating a hydrodynamic diameter of $25 \pm 8 \text{ nm}$. (D) XRD spectra of (top) oven-dried and (bottom) freeze-dried LaNiO_3 . NiO phase impurities are marked with a star.

To obtain an aqueous dispersion of amorphous perovskite precursor nanoparticles, metal nitrates of La^{3+} and Ni^{2+} were hydrolyzed rapidly in the presence of a capping ligand, tetrapropylammonium bromide (TPAB), as described in detail in the Supporting Information. This approach created amorphous particles of La and Ni hydroxides with a hydrodynamic diameter of 25 nm (peak width, $\pm 8 \text{ nm}$), as shown via DLS in Figure 1C. To promote complete and rapid hydrolysis of both La and Ni nitrates while maintaining a constant pH during the reaction,¹⁸ an excess volume of pH 14 tetramethylammonium hydroxide (TMAOH) was used. The capping ligand TPAB provided colloidal stabilization through a combination of electrostatic and steric repulsion.²⁵ Without TPAB, the particles agglomerated, even after sonication, presumably leading to lower phase purity and lower surface

areas, as seen previously in a similar synthesis.²¹ Prior to calcination, the amorphous particle dispersions were either freeze-dried by a combination of thin film freezing followed by lyophilization or dried in an oven at 120°C for $\sim 1 \text{ h}$. In the freeze-drying process, droplets of the amorphous particle dispersion were spread onto the surface of a rotating metal drum at -78°C and frozen into a thin film ($\sim 100 \text{ nm}$ thick) at fast freezing rates ($\sim 100 \text{ K/s}$).²⁶ The time scale for freezing (order of milliseconds) was sufficiently fast to prevent significant growth of the amorphous nanoparticles. After lyophilization, a fluffy powder was produced, with open flocs of the nanoparticles with a low fractal dimension, consistent with numerous related studies of organic substances.^{27,28} In contrast, oven drying of the aqueous dispersion led to gelation, whereby the capillary forces produced somewhat more dense aggregates. In essence, the frozen freeze-dried material may be considered to be closer to the rapid-diffusion-limited aggregation regime, whereas the slowly dried material is closer to the reaction-limited regime, where particles explore a greater number of configurations to lower the surface area, resulting in a larger aggregate density.²⁹

After particles formed via reverse-phase precipitation were calcined in air at 700°C for 4 h to form crystalline LaNiO_3 , the morphology of the oven-dried precursor was aggregates of sintered primary nanoparticles, with modest coalescence and particle growth, as shown by the SEM images in the Supporting Information (Figure S1C,D). For the freeze-dried dispersions, the amount of coalescence and growth was less prevalent, resulting in aggregates of ~ 20 – 50 nm partially coalesced primary nanoparticles, as seen in Figures 1A and S1A,B (Supporting Information). It is possible that the large interparticle spacing in the highly open, low fractal dimension aggregates suppressed sintering despite the 700°C calcination temperature. Remarkably, the original 25 nm precursor ($33 \text{ m}^2/\text{g}$ for individual spheres) particles grew only modestly during calcination. The nitrogen adsorption (BET)-measured surface areas of the freeze-dried and oven-dried samples, after calcination, were 11 and $6 \text{ m}^2/\text{g}$, respectively (Table S1, Figure S2, Supporting Information). Both catalysts were comprised of an essentially phase-pure crystalline rhombohedral LaNiO_3 phase, as shown in the XRD spectra in Figure 1D. The slightly impure phase identified in both samples was NiO as the peaks were barely visible at 2θ s of 35° , 42.5° , and 62.5° . According to Scherrer analysis performed on the most intense reflection due to a single-crystalline plane, $\{024\}$ for LaNiO_3 , similar crystallite sizes of $\sim 15 \text{ nm}$ were calculated for the two drying approaches. Note that crystallite size is not indicative of particle size, surface area, or resulting catalytic activities.

The phase purity and relatively high surface area after calcination may be attributed to rapid and simultaneous reduction of both metal nitrates to form nanoparticle precursors, leading to an appropriate level of intermixing of the metal hydroxides. Instantaneously, upon adding the nitrates into the pH 14 solution in this reverse-phase precipitation reaction,^{18,25} a light green dispersion was visible. The burst nucleation followed by arrested growth led to 25 nm nanoparticles with apparently adequate intermixing of both metal hydroxides. Thus, this approach overcomes the dissimilar hydrolysis rate constants for La^{3+} and Ni^{2+} , which differ by up to almost 1 order of magnitude at a lower pH $< \sim 10$.²² This is in contrast to normal-phase coprecipitation, whereby the pH immediately decreases upon dropwise addition of base into a solution of dissolved metal salts, which could lead to phase

impurities, as has been seen previously for coprecipitation of other systems.^{22,30} It is likely that hydrolysis of the less reactive component lags nucleation and growth of the more reactive one. Thus, the burst nucleation and high pH in the reverse-phase method enable rapid hydrolysis of both metal nitrates to form amorphous composite nanoparticles that upon calcination, formed phase-pure nanocrystal aggregates.

To probe the physical and chemical properties of the catalyst surface, the O 1s core-level spectrum of unsupported nsLaNiO₃ was collected via high-resolution XPS and deconvoluted in the same manner, as reported by Mickevicius et al.³¹ The spectrum, shown in Figure 1B, contains four distinct species of oxygen corresponding to lattice oxygen in lanthanum oxide (528.3 eV) and nickel oxide (529.3 eV), lanthanum and nickel hydroxides (531.4 eV), and adsorbed water (533.2 eV). Upon deconvolution, it was found that the catalyst surface was significantly hydroxylated (~65 rel. atom %). It has been previously shown that the least energetically favorable step of the OER is either chemisorbed OOH⁻ formation or oxidation of surface OH⁻.^{32–34} Furthermore, it has been proposed that the concentration of lattice hydroxide directly affects the rate at which surface peroxide forms during the OER.³⁵ Thus, the presence of lattice hydroxide is expected to have a positive effect on measured OER activity.

To determine the effect of perovskite morphology and surface area on OER activity, polarization curves were measured in Ar-saturated 0.1 M KOH at 900 rpm (Figure 2A). At 1.63 V versus the reversible hydrogen electrode (RHE), or a 0.4 V overpotential, the total OER mass activity for unsupported nsLaNiO₃ was 24 mA/mg, nearly two times greater than that for the lower surface area oven-dried LaNiO₃ (13 mA/mg), seen in Figure 2A,B. For the unsupported

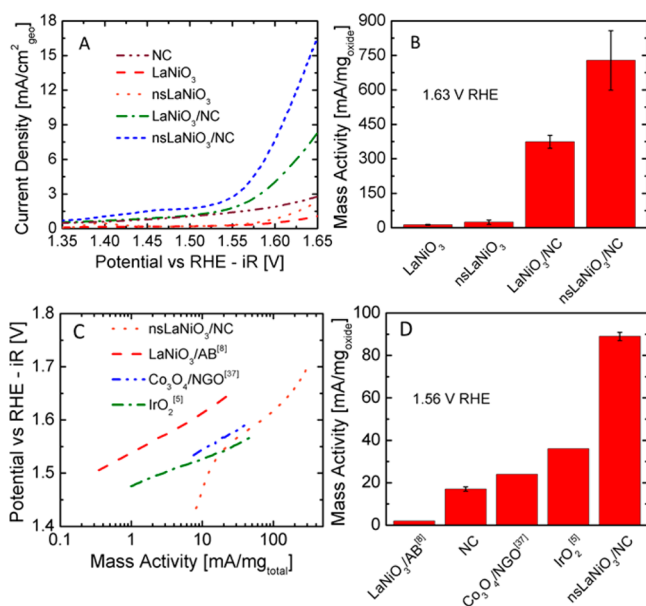


Figure 2. OER activity trends in (A,B) Ar-saturated 0.1 M KOH at 900 rpm and 50 mV/s and (C,D) O₂-saturated 0.1 M KOH at 1600 rpm and 10 mV/s. (A) Linear sweep voltammogram and (B) selected oxide mass activities calculated at 1.63 V from data in (A). (C) Tafel plot comparing nsLaNiO₃ mass activity in O₂-saturated 0.1 M KOH to other leading OER catalysts and (D) oxide (total in the case of NC) mass activity in O₂-saturated 0.1 M KOH. Note that at potentials > 1.53 V, nsLaNiO₃/NC has considerably higher OER activity than the pure NC.

perovskites, such low activities are expected given their lower conductivities relative to the high surface area (~1080 m²/g, Figure S3 (Supporting Information)), conductive NC support.³⁶ The carbon support provides a conductive network by which the catalyst is electrically wired to the electrode, while the bare catalyst is only in electrical contact with the electrode by point contacts. For nsLaNiO₃ supported on NC (nsLaNiO₃/NC), the mass activity was 728 mA/mg_{oxide}, again nearly two times higher than the value of 374 mA/mg_{oxide} obtained for the lower surface area LaNiO₃/NC catalyst.

In Figure 2C,D, the OER total mass activities (representative polarization curve shown in Figure S4, Supporting Information) for nsLaNiO₃/NC are comparable to those of a leading benchmark catalyst, IrO₂.⁵ Furthermore, they are well above recently reported values for coprecipitated LaNiO₃ supported on acetylene black (AB)⁸ and Co₃O₄ supported on nitrogen-doped reduced graphene oxide (Co₃O₄/NGO).³⁷ In these comparisons, the electrolyte was saturated with oxygen. At a chosen potential of 1.56 V, the nsLaNiO₃/NC activity was already markedly above that of the NC baseline, as is evident in Figure 2C. Remarkably, on an oxide mass basis, the activity for nsLaNiO₃/NC (89 mA/mg_{oxide}) reached 2.5× that of a leading benchmark catalyst, 6 nm IrO₂ (36 mA/mg_{oxide}). Because the surface area to mass ratio of IrO₂ is 71 m²/g, compared to 11 m²/g for nsLaNiO₃/NC, the apparent specific activity (based on surface area measurement via BET) was ~450 μA/cm²_{oxide}, compared to ~50 μA/cm²_{oxide} for IrO₂. The value for the former was corrected for the small NC current contribution. Relative to literature values reported for LaNiO₃ synthesized via normal-phase coprecipitation (3.5 m²/g) and supported on AB, the activity of nsLaNiO₃/NC is ~45 times higher at 1.56 V. The oxide mass activity of nsLaNiO₃/NC is ~3.8 times that of a highly active 6 nm Co₃O₄ supported on nitrogen-doped graphene oxide (24 mA/mg_{oxide}). Additionally, the mass activity is ~18 times higher than that reported in a recent study of the most OER active perovskite, Ba_{0.5}Sr_{0.5}Co_{0.8}Fe_{0.2}O₃ (0.2 m²/g),⁸ despite its high specific activity of ~2500 μA/cm²_{oxide}.

The high mass activity for nsLaNiO₃/NC partially reflects the phase-pure high surface area crystalline LaNiO₃ nanoparticle aggregates, enabled by the precursor synthetic approach. The large numbers of facets in the nanoparticle domains and the regions between them offer the possibility of more access to most active surfaces, such as the {100} planes in LaNiO₃.³⁵ The morphology of thin layers of nanocrystal aggregates on the carbon substrate is also beneficial, for example, as seen for MnO_x³⁸ and highly active oxyhydroxide thin films.³⁹

To further understand the mechanism responsible for the high electrocatalytic activity reported herein, it is necessary to reexamine the role of lattice hydroxides in the OER. Lattice oxygen in LaNiO₃ is weakly bound^{40,41} and can be considered protonated such that it contributes a lattice hydroxide to the formation of OOH⁻ during the OER.^{31,35,42} Lattice oxygen directly participating in the OER has been observed for similar oxides such as Li-NiO, IrO₂, and RuO₂.^{43–45} Figure S6 (Supporting Information) depicts this OER cycle, wherein the formations of OH, O²⁻, and OOH⁻ intermediates are reconciled with the utilization of lattice (hydr)oxide in the formation of surface-adsorbed hydroperoxide. This cycle rationalizes the unusually high OER mass activities observed herein. The rate-determining step of the OER on LaNiO₃ (Figure S6 (Supporting Information), step 3) is governed by the concentration of lattice (hydr)oxide species that participate

in the formation of the O–O bond in hydroperoxide; thus, the high lattice (hydr)oxide concentration of nsLaNiO₃ increases the rate at which HOO[−] forms and consequently the rate at which the OER proceeds.^{32–35} Furthermore, as lattice (hydr)oxides are oxidized to form hydroperoxide, a positively charged vacancy is left behind. This lattice oxygen vacancy is rapidly replenished from the bulk electrolyte (Figure S6 (Supporting Information), step L),⁴² resulting in the lack of hysteresis observed during OER testing (Figure S4, Supporting Information).

These perovskite catalysts also displayed appreciable activity for the ORR. Polarization curves for ORR in oxygen-saturated 0.1 M KOH at 1600 rpm and 5 mV/s are shown in Figure 3A,

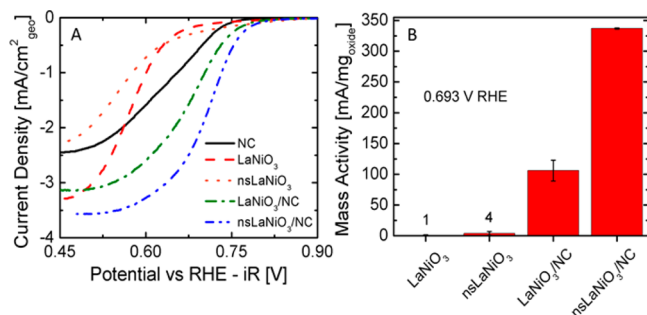


Figure 3. ORR activity trends in O₂-saturated 0.1 M KOH at 1600 rpm. (A) Polarization curves for the ORR, including pure NC, and supported/unsupported LaNiO₃/nsLaNiO₃. (B) Oxide mass activities taken at 0.693 V, showing high mass activity for the nsLaNiO₃/NC catalyst.

with activity measurements taken at 0.693 V. Low activities were observed for unsupported LaNiO₃ and nsLaNiO₃, 1 and 4 mA/mg, respectively. As for the OER, this was likely due to the lower conductivity of the pure oxide. However, when LaNiO₃ and nsLaNiO₃ were supported on NC, the half-wave potential shifted >100 mV positive and resulted in significantly higher activities of 32 and 101 mA/mg_{total}, respectively. The activity increased more than an order of magnitude for the ORR, as was also seen for the OER. The activity of nsLaNiO₃/NC reached 337 mA/mg_{oxide}, ~3 times higher than that for the oven-dried LaNiO₃/NC (Figure 3B), similar to the observed increase in BET surface area as summarized in Table S1 (Supporting Information). NC further contributes to the activity due most likely to the presence of pyridinic functional groups in the surface, as shown by XPS in Figure S7 (Supporting Information).^{46,47}

As a measure of the overall bifunctionality of the catalyst, we determined the difference in potential between the ORR at −3 mA/cm² and OER at 10 mA/cm² (ΔE), current densities of practical importance for electrochemical and photoelectrochemical applications.³⁸ ΔE is simply the sum of the overpotentials for the two reactions. Table 1 shows the excellent bifunctional character ($\Delta E = 1.02$ V) of the nsLaNiO₃/NC catalyst, which is exceeded by 100 mV only

for the ORR-active precious metal Ir ($\Delta E = 0.92$ V)³⁸ that also forms an OER-active oxide at anodic potentials.

Remarkably, the ΔE of 1.02 for nsLaNiO₃ is significantly better than that for Pt/C ($\Delta E = 1.16$ V),³⁸ a leading ORR catalyst but a poor OER catalyst. While it has been demonstrated that phase purity is important for achieving high bifunctional character, the specific interactions between the perovskite catalyst and NC are not well understood. Electronic and ensemble effects, like those recently observed for bimetallic and mixed metal–metal oxide catalyst,^{48,49} could be contributing to the high activities reported here. Additionally, the specific interactions between the perovskite catalyst and NC likely play a much smaller secondary role, such as H₂O₂ disproportionation and improved support hydrophilicity. Future work will explore the interplay between these various effects.

In conclusion, LaNiO₃ nanocrystalline aggregates on NC exhibit extremely high activity for the OER and strong OER/ORR bifunctional character as a result of high phase purity, lattice hydroxylation, and increased surface area. This bifunctional character is crucial to the development of inexpensive aqueous metal–air batteries, fuel cells, and electrolyzers. This highly active morphology is produced by rapid, simultaneous hydrolysis of La³⁺ and Ni²⁺ nitrates during reverse-phase arrested growth precipitation, followed by rapid drying. This synthetic concept to generate precursors that are calcined to form phase-pure nanocrystalline aggregates is general and thus a directly applicable route to prepare a wide variety of nonprecious metal nanocrystalline perovskites as highly active catalysts.

EXPERIMENTAL METHODS

Chemicals. All chemicals were used as received. Anhydrous ethanol and 5 wt % Nafion solution in lower alcohols were purchased from Sigma-Aldrich. Nickel(II) nitrate hexahydrate (99%), lanthanum(III) nitrate hexahydrate (99.999%), tetrapropylammonium bromide (TPAB, 98%), tetramethylammonium hydroxide pentahydrate (TMAOH, 99%), 2-propanol, and potassium hydroxide were obtained from Fisher Scientific, and ethanol (Absolute 200 proof) was from Aaper alcohol. Millipore high-purity water (18 M Ω) was used. Oxygen (research grade, 99.999% purity) and argon (research grade, 99.999% purity) were obtained from Praxair. Nitrogen-doped carbon (NC) was prepared as reported elsewhere.⁵⁰

Synthesis of the Nanostructured LaNiO₃ Catalyst (nsLaNiO₃). Mixed metal hydroxide particles were prepared by reverse hydrolysis of La and Ni nitrates in the presence of an equimolar amount of TPAB dissolved into 1 wt % TMAOH. In a typical synthesis, 50 mL of a mixed metal nitrates (~10 mM) solution was added dropwise (~2 mL/min) to 200 mL of vigorously stirred TMAOH. The solution was left stirring for 30 min, and the resulting suspension was washed with DI water via centrifugation three times, followed by probe sonication. The resulting washed particle solution was frozen into a thin film and then lyophilized at −10 °C and a fixed pressure of ~50

Table 1. Assessment of Catalyst Bifunctionality for nsLaNiO₃/NC and Other Benchmarks

catalyst	ORR potential (V) vs RHE @ −3 mA/cm ²	OER potential (V) vs RHE @ 10 mA/cm ²	ΔE (V)
nsLaNiO ₃ /NC	0.64	1.66	1.02
20% Ir/C ³⁸	0.69	1.61	0.92
20% Pt/C ³⁸	0.86	2.02	1.16

mTorr for 20 h. The lyophilized powder was calcined at 700 °C for 4 h under flowing dehumidified air. Following calcination, all particles were washed with EtOH and filtered to obtain the final nsLaNiO₃ catalyst. Synthesis of LaNiO₃ was identical to that of nsLaNiO₃, except that the washed hydroxide gel was spread over a glass dish and dried at 120 °C under air for a minimum of 1 h prior to calcination, rather than thin film freezing followed by lyophilization.

Materials Characterization. The hydrodynamic diameter (D_H) of as-synthesized hydrolysis particles was measured via dynamic light scattering (DLS, Brookhaven ZetaPALS instrument) and fit with the CONTIN routine. Structural information of as-calcined oxides was obtained using wide-angle X-ray diffraction (Bruker Nokius AXS D8 Advance) emitting Cu K α radiation (1.54 Å) and the background removed with JADE software (Molecular Diffraction Inc.). Surface morphologies of the perovskite catalysts were observed using scanning electron microscopy (SEM, Hitachi S-5500), while surface areas were quantified using nitrogen sorption (Quantachrome Instruments NOVA 2000) at 77 K. Chemical states were probed by X-ray photoelectron spectroscopy (XPS, Kratos AXIS Ultra DLD) using a monochromatic Al X-ray source (Al α , 1.4866 keV).

Electrochemical Characterization. Electrochemical testing was performed on either a CH Instruments CHI832a or a Metrohm Autolab PGSTAT302N potentiostat, both equipped with high speed rotators from Pine Instruments. All testing was done at room temperature in 0.1 M KOH (measured pH \approx 12.6), and all data were iR corrected (50 Ω) after testing. Electrolyte resistance was found prior to testing by a combination of the current-interrupt and positive feedback methods. Each test was performed in a standard three-electrode cell using a Hg/HgO (1 M KOH) reference electrode, a Pt wire counter electrode, and a film of catalyst ink on glassy carbon as the working electrode. All potentials are reported versus the regular hydrogen electrode (RHE), which was shifted +0.843 V versus Hg/HgO (Hg/HgO (1 M KOH) + 0.1 V = NHE; NHE + 0.059 \times pH = RHE). Catalyst inks were prepared by addition of 1 mL of NaOH-neutralized 0.05 wt % Nafion solution¹⁹ to 1 mg of catalyst powder and bath sonicated for 30 min. Then, 10 μ L of ink was placed onto a clean 5 mm (0.196 cm²) glassy carbon electrode and left to dry under a glass jar. The activity of the catalyst toward the ORR was determined by rotating the electrode at 1600 rpm in O₂-saturated media and performing a linear potential sweep at 5 mV/s. Kinetic currents were calculated according to the Koutecky–Levich equation from the resulting polarization curves. All ORR mass activities reported herein are averages from cathodic scans taken of multiple electrodes. Oxygen evolution activities were quantified in either O₂-saturated or deoxygenated media by performing anodic potential sweeps at 10 and 50 mV/s, respectively. All electrochemical tests were performed on freshly prepared electrodes, except for deoxygenated OER tests. These tests were conducted on the same electrode following O₂-saturated ORR measurements. All OER mass activities reported herein are averages from anodic scans taken of multiple electrodes.

■ ASSOCIATED CONTENT

■ Supporting Information

Detailed experimental methods, electron microscopy images, summary of catalyst surface areas, nitrogen adsorption curves, OER polarization curve, and XPS spectra for the N 1s core region. This material is available free of charge via the Internet at <http://pubs.acs.org>.

■ AUTHOR INFORMATION

Corresponding Author

*E-mail: stevenson@cm.utexas.edu (K.J.S.); kpj@che.utexas.edu (K.P.J.).

Author Contributions

[†]The manuscript was written through contributions of all authors. All authors have given approval to the final version of the manuscript. W.G.H. and D.A.S. contributed equally.

Notes

The authors declare no competing financial interest.

■ ACKNOWLEDGMENTS

Financial support for this work was provided by the R. A. Welch Foundation (Grants F-1529 and F-1319). The Kratos XPS was funded by the NSF under Grant CHE-0618242. We would also like to thank Karen Ann Li for helpful discussions.

■ REFERENCES

- (1) Bidault, F.; Brett, D. J. L.; Middleton, P. H.; Brandon, N. P. Review of Gas Diffusion Cathodes for Alkaline Fuel Cells. *J. Power Sources* **2009**, *187*, 39–48.
- (2) Cheng, F. Y.; Chen, J. Metal–Air Batteries: From Oxygen Reduction Electrochemistry to Cathode Catalysts. *Chem. Soc. Rev.* **2012**, *41*, 2172–2192.
- (3) Neburchilov, V.; Wang, H.; Martin, J. J.; Qu, W. A Review on Air Cathodes for Zinc–Air Fuel Cells. *J. Power Sources* **2010**, *195*, 1271–1291.
- (4) Harting, K.; Kunz, U.; Turek, T. Zinc–Air Batteries: Prospects and Challenges for Future Improvement. *Z. Phys. Chem.* **2012**, *226*, 151–166.
- (5) Lee, Y.; Suntivich, J.; May, K. J.; Perry, E. E.; Shao-Horn, Y. Synthesis and Activities of Rutile IrO₂ and RuO₂ Nanoparticles for Oxygen Evolution in Acid and Alkaline Solutions. *J. Phys. Chem. Lett.* **2012**, *3*, 399–404.
- (6) Spendelov, J. S.; Wieckowski, A. Electrocatalysis of Oxygen Reduction and Small Alcohol Oxidation in Alkaline Media. *Phys. Chem. Chem. Phys.* **2007**, *9*, 2654–2675.
- (7) Suntivich, J.; Gasteiger, H. A.; Yabuuchi, N.; Nakanishi, H.; Goodenough, J. B.; Shao-Horn, Y. Design Principles for Oxygen-Reduction Activity on Perovskite Oxide Catalysts for Fuel Cells and Metal–Air Batteries. *Nat. Chem.* **2011**, *3*, 546–550.
- (8) Suntivich, J.; May, K. J.; Gasteiger, H. A.; Goodenough, J. B.; Shao-Horn, Y. A Perovskite Oxide Optimized for Oxygen Evolution Catalysis from Molecular Orbital Principles. *Science* **2011**, *334*, 1383–1385.
- (9) Karlsson, G. Reduction of Oxygen on LaNiO₃ in Alkaline-Solution. *J. Power Sources* **1983**, *10*, 319–331.
- (10) Trasatti, S. Electrocatalysis by Oxides — Attempt at a Unifying Approach. *J. Electroanal. Chem.* **1980**, *111*, 125–131.
- (11) Twu, J.; Gallagher, P. K. In *Properties and Applications of Perovskite-Type Oxides*; Tejuca, L. G.; Fierro, J. L. G., Ed.; Marcel Dekker, Inc.: New York, 1993.
- (12) Sunarso, J.; Torriero, A. A. J.; Zhou, W.; Howlett, P. C.; Forsyth, M. Oxygen Reduction Reaction Activity of La-Based Perovskite Oxides in Alkaline Medium: A Thin-Film Rotating Ring-Disk Electrode Study. *J. Phys. Chem. C* **2012**, *116*, 5827–5834.
- (13) Chen, Z.; Yu, A. P.; Higgins, D.; Li, H.; Wang, H. J.; Chen, Z. W. Highly Active and Durable Core-Corona Structured Bifunctional Catalyst for Rechargeable Metal–Air Battery Application. *Nano Lett.* **2012**, *12*, 1946–1952.
- (14) Zhuang, S. X.; Huang, C. H.; Huang, K. L.; Hu, X.; Tu, F. Y.; Huang, H. X. Preparation of Homogeneous Nanoporous La_{0.6}Ca_{0.4}CoO₃ for Bi-Functional Catalysis in an Alkaline Electrolyte. *Electrochem. Commun.* **2011**, *13*, 321–324.

- (15) Haider, M. A.; Capizzi, A. J.; Murayama, M.; McIntosh, S. Reverse Micelle Synthesis of Perovskite Oxide Nanoparticles. *Solid State Ionics* **2011**, *196*, 65–72.
- (16) Yuasa, M.; Sakai, G.; Shimanoe, K.; Teraoka, Y.; Yamazoe, N. Exploration of Reverse Micelle Synthesis of Carbon-Supported LaMnO_3 . *J. Electrochem. Soc.* **2004**, *151*, A1477–A1482.
- (17) Yuasa, M.; Shimanoe, K.; Teraoka, Y.; Yamazoe, N. High-Performance Oxygen Reduction Catalyst Using Carbon-Supported La–Mn-Based Perovskite-Type Oxide. *Electrochem. Solid St.* **2011**, *14*, A67–A69.
- (18) Imaizumi, S.; Shimanoe, K.; Teraoka, Y.; Miura, N.; Yamazoe, N. Preparation of Carbon-Supported Perovskite-Type Oxides $\text{LaMn}_{1-y}\text{Fe}_y\text{O}_{3+\delta}$ Based on Reverse Homogeneous Precipitation Method. *J. Electrochem. Soc.* **2004**, *151*, A1559–A1564.
- (19) Suntivich, J.; Gasteiger, H. A.; Yabuuchi, N.; Shao-Horn, Y. Electrocatalytic Measurement Methodology of Oxide Catalysts Using a Thin-Film Rotating Disk Electrode. *J. Electrochem. Soc.* **2010**, *157*, B1263–B1268.
- (20) Yuasa, M.; Nishida, M.; Kida, T.; Yamazoe, N.; Shimanoe, K. Bi-Functional Oxygen Electrodes Using $\text{LaMnO}_3/\text{LaNiO}_3$ for Rechargeable Metal–Air Batteries. *J. Electrochem. Soc.* **2011**, *158*, A605–A610.
- (21) Ovenstone, J.; Chan, K. C.; Ponton, C. B. Hydrothermal Processing and Characterisation of Doped Lanthanum Chromite for Use in Sofcs. *J. Mater. Sci.* **2002**, *37*, 3315–3322.
- (22) Shao, Z. P.; Zhou, W.; Zhu, Z. H. Advanced Synthesis of Materials for Intermediate-Temperature Solid Oxide Fuel Cells. *Prog. Mater. Sci.* **2012**, *57*, 804–874.
- (23) Bhalla, A. S.; Guo, R. Y.; Roy, R. The Perovskite Structure — A Review of Its Role in Ceramic Science and Technology. *Mater. Res. Innovations* **2000**, *4*, 3–26.
- (24) Patzke, G. R.; Zhou, Y.; Kontic, R.; Conrad, F. Oxide Nanomaterials: Synthetic Developments, Mechanistic Studies, and Technological Innovations. *Angew. Chem., Int. Ed.* **2011**, *50*, 826–859.
- (25) Teraoka, Y.; Nanri, S.; Moriguchi, I.; Kagawa, S.; Shimanoe, K.; Yamazoe, N. Synthesis of Manganite Perovskites by Reverse Homogeneous Precipitation Method in the Presence of Alkylammonium Cations. *Chem. Lett.* **2000**, 1202–1203.
- (26) Bennett, T.; Poulikakos, D. Splat-Quench Solidification: Estimating the Maximum Spreading of a Droplet Impacting a Solid Surface. *J. Mater. Sci.* **1993**, *28*, 963–970.
- (27) Engstrom, J. D.; Lai, E. S.; Ludher, B. S.; Chen, B.; Milner, T. E.; Williams, R. O.; Kitto, G. B.; Johnston, K. P. Formation of Stable Submicron Protein Particles by Thin Film Freezing. *Pharm. Res.* **2008**, *25*, 1334–1346.
- (28) Overhoff, K. A.; Engstrom, J. D.; Chen, B.; Scherzer, B. D.; Milner, T. E.; Johnston, K. P.; Williams, Iii, R. O. Novel Ultra-Rapid Freezing Particle Engineering Process for Enhancement of Dissolution Rates of Poorly Water-Soluble Drugs. *Eur. J. Pharm. Biopharm.* **2007**, *65*, 57–67.
- (29) Lin, M. Y.; Lindsay, H. M.; Weitz, D. A.; Ball, R. C.; Klein, R.; Meakin, P. Universality in Colloid Aggregation. *Nature* **1989**, *339*, 360–362.
- (30) Cushing, B. L.; Kolesnichenko, V. L.; O'Connor, C. J. Recent Advances in the Liquid-Phase Syntheses of Inorganic Nanoparticles. *Chem. Rev.* **2004**, *104*, 3893–3946.
- (31) Mickevicius, S.; Grebinkij, S.; Bondarenka, V.; Vengalis, B.; Sliuziene, K.; Orłowski, B. A.; Osinniy, V.; Drube, W. Investigation of Epitaxial LaNiO_{3-x} Thin Films by High-Energy XPS. *J. Alloys Compd.* **2006**, *423*, 107–111.
- (32) Dau, H.; Limberg, C.; Reier, T.; Risch, M.; Roggan, S.; Strasser, P. The Mechanism of Water Oxidation: From Electrolysis via Homogeneous to Biological Catalysis. *ChemCatChem* **2010**, *2*, 724–761.
- (33) Man, I. C.; Su, H. Y.; Calle-Vallejo, F.; Hansen, H. A.; Martinez, J. I.; Inoglu, N. G.; Kitchin, J.; Jaramillo, T. F.; Nørskov, J. K.; Rossmeisl, J. Universality in Oxygen Evolution Electrocatalysis on Oxide Surfaces. *ChemCatChem* **2011**, *3*, 1159–1165.
- (34) Rossmeisl, J.; Qu, Z. W.; Zhu, H.; Kroes, G. J.; Nørskov, J. K. Electrolysis of Water on Oxide Surfaces. *J. Electroanal. Chem.* **2007**, *607*, 83–89.
- (35) Bockris, J. O.; Otagawa, T. Mechanism of Oxygen Evolution on Perovskites. *J. Phys. Chem.* **1983**, *87*, 2960–2971.
- (36) Karlsson, G. Perovskite Catalysts for Air Electrodes. *Electrochim. Acta* **1985**, *30*, 1555–1561.
- (37) Liang, Y. Y.; Li, Y. G.; Wang, H. L.; Zhou, J. G.; Wang, J.; Regier, T.; Dai, H. J. Co_3O_4 Nanocrystals on Graphene as a Synergistic Catalyst for Oxygen Reduction Reaction. *Nat. Mater.* **2011**, *10*, 780–786.
- (38) Gorlin, Y.; Jaramillo, T. F. A Bifunctional Nonprecious Metal Catalyst for Oxygen Reduction and Water Oxidation. *J. Am. Chem. Soc.* **2010**, *132*, 13612–13614.
- (39) Trotochaud, L.; Ranney, J. K.; Williams, K. N.; Boettcher, S. W. Solution-Cast Metal Oxide Thin Film Electrocatalysts for Oxygen Evolution. *J. Am. Chem. Soc.* **2012**, *134*, 17253–17261.
- (40) Konyshova, E.; Irvine, J. T. S. Thermochemical and Structural Stability of A- and B-Site-Substituted Perovskites in Hydrogen-Containing Atmosphere. *Chem. Mater.* **2009**, *21*, 1514–1523.
- (41) Subbaraman, R.; Tripkovic, D.; Chang, K.-C.; Strmcnik, D.; Paulikas, A. P.; Hirunsit, P.; Chan, M.; Greeley, J.; Stamenkovic, V.; Markovic, N. M. Trends in Activity for the Water Electrolyser Reactions on 3d $\text{M}(\text{Ni}, \text{Co}, \text{Fe}, \text{Mn})$ Hydr(Oxy)Oxide Catalysts. *Nat. Mater.* **2012**, *11*, 550–557.
- (42) Boehm, H. P. Acidic and Basic Properties of Hydroxylated Metal Oxide Surfaces. *Discuss. Faraday Soc.* **1971**, *52*, 264–275.
- (43) Lee, C.; Riga, A.; Yeager, E. In *Mass Transport Phenomena in Ceramics*; Gordon, R. S., Cooper, A. R., Heuer, A. H., Eds.; Plenum Press: New York, 1975; p 489.
- (44) Fierro, S.; Nagel, T.; Baltruschat, H.; Comninellis, C. Investigation of the Oxygen Evolution Reaction on Ti/IrO_2 Electrodes Using Isotope Labelling and on-Line Mass Spectrometry. *Electrochem. Commun.* **2007**, *9*, 1969–1974.
- (45) Wohlfahrt-Mehrens, M.; Heitbaum, J. Oxygen Evolution on Ru and RuO_2 Electrodes Studied Using Isotope Labelling and on-Line Mass Spectrometry. *J. Electroanal. Chem. Interfacial Electrochem.* **1987**, *237*, 251–260.
- (46) Maldonado, S.; Stevenson, K. J. Influence of Nitrogen Doping on Oxygen Reduction Electrocatalysis at Carbon Nanofiber Electrodes. *J. Phys. Chem. B* **2005**, *109*, 4707–4716.
- (47) Wiggins-Camacho, J. D.; Stevenson, K. J. Mechanistic Discussion of the Oxygen Reduction Reaction at Nitrogen-Doped Carbon Nanotubes. *J. Phys. Chem. C* **2011**, *115*, 20002–20010.
- (48) Slanac, D. A.; Hardin, W. G.; Johnston, K. P.; Stevenson, K. J. Atomic Ensemble and Electronic Effects in Ag-Rich AgPd Nanoalloy Catalysts for Oxygen Reduction in Alkaline Media. *J. Am. Chem. Soc.* **2012**, *134*, 9812–9819.
- (49) Slanac, D. A.; Lie, A.; Paulson, J. A.; Stevenson, K. J.; Johnston, K. P. Bifunctional Catalysts for Alkaline Oxygen Reduction Reaction Via Promotion of Ligand and Ensemble Effects at Ag/MnO_x Nanodomains. *J. Phys. Chem. C* **2012**, *116*, 11032–11039.
- (50) Wang, X. Q.; Lee, J. S.; Zhu, Q.; Liu, J.; Wang, Y.; Dai, S. Ammonia-Treated Ordered Mesoporous Carbons as Catalytic Materials for Oxygen Reduction Reaction. *Chem. Mater.* **2010**, *22*, 2178–2180.